

Research Article

Cyclic Behavior of Steel Beam to CFT Column Connections with Gusset Plates

Peng Wang ¹, Zhan Wang ^{1,2}, Jianrong Pan ^{1,2}, Yanjun Zheng ¹ and Deming Liu ¹

¹School of Civil Engineering and Transportation, South China University of Technology, Guangzhou 510641, China

²State Key Laboratory of Subtropical Building Science, South China University of Technology, Guangzhou 510641, China

Correspondence should be addressed to Jianrong Pan; ctjrpan@scut.edu.cn

Received 5 June 2019; Accepted 21 October 2019; Published 16 November 2019

Academic Editor: Jiang Jin

Copyright © 2019 Peng Wang et al. This is an open access article distributed under the Creative Commons Attribution License, which permits unrestricted use, distribution, and reproduction in any medium, provided the original work is properly cited.

Beam-brace-CFT (concrete-filled tubular) column connections provide excellent performance in resisting seismic loads in high-risk areas. However, the load transmission mechanism of this type of connection still remains unclear, and there is a lack of study on it. Therefore, in this paper, the mechanical behavior of beam-brace-CFT column (BBC) connections penetrated by gusset plates was evaluated through experiments and finite element analysis to resolve this issue. The failure modes, strength, stiffness, ductility, and energy dissipation of this type of connection were studied. Experiment results indicated that the gusset plates in BBC (beam-brace-CFT) connections could effectively move the plastic hinge on beam away from the column face, reduce the strain concentration between the beam end and column face, and notably improve the hysteretic behavior; the plastic rotation was able to achieve at least 4% story drift angle before 20% strength degradation. Numerical studies were carried out and validated by experiment results, and then the influence of the weld length and strengthening methods were investigated; some improvement of design suggestions was proposed.

1. Introduction

For high-rise buildings, braced frame is a popular choice to resist the earthquake for its high lateral stiffness [1, 2]. Moreover, in braced frame systems, concrete-filled tubular (CFT) columns are also commonly used because of their favorable strength and stiffness; the concrete fill in CFT columns not only contributes stiffness and compressive strength but also restrains the steel tube from local buckling [3–5]. On the contrary, the steel tubes can be set as the shuttering of concrete so the labor cost could be decreased during the construction process. However, when connecting CFT columns to beams and braces together, several issues should not be ignored [6–9]. For example, the connections should be capable to transfer all applied loads as expectation; the loads must be reasonably distributed in the steel tube and the concrete infill to ensure the composite action, and the connections must possess enough deformation ability to maintain the ductility of the whole structure.

Current design codes such as Eurocode 4 [10], AISC Specification [11], and CIDECT [12] provide different approaches to calculate the load distribution among the members associated with connections. One popular CFT column connection is using an internal diaphragm [13] and through diaphragm [14–16] which requires extra complete penetration welds around the perimeter of the tube at the beam-column intersection and the beam flange. The way that the diaphragm welded in the connection is too difficult, costly, and time consuming to be realized in practical engineering. Recently, a more convenient and economic BBC connection was studied by Macrae et al. [17], Hassan et al. [18], and Hu et al. [19], in which the braces and beams are attached to a vertical gusset plate that penetrates through the circular CFT column, and the force transfers through friction and bearing mechanism at the bottom of the plate. The construction of penetrating gusset plates increases the resistance and ductility of connections, ensures the composite action, and restrains the interface slip within the CFT column between steel tubes and concrete infill. However, these

researches did not focus on some significant seismic design issues on braced frame connections, such as the construction details of beams, gusset plates, and CFT columns.

Previous seismic record and numerical analysis data show that the secondary lateral force resisting capacity plays an important role in collapse resistance in low-ductility structures under seismic activity. During the earthquake in Northridge, lots of steel frame structures still stayed up, although their lateral resisting systems were damaged by seismic action, which owed to the inherent reserve capacity within structures. This reserve capacity comes from the ductility of the joint, which is especially critical in the seismic design of moderate earthquake areas, and it should not be classified into the initial lateral resistance system [20–22]. Although this capacity would take function in the severe earthquake zone, it works better in low and moderate earthquake areas.

As mentioned above, beam-to-column connections which have certain flexural resistance in CBFs provide significant reserve capacity after the failure of the braces. But prior researches on the flexural behavior of concentrically braced frame (CBF) connections are limited to the studies of Kishiki et al. [23] and Stoakes and Fahnstock [21]. Moreover, despite the convenient and economical penetrated gusset plate connection employed in the BBC-CBF system, previous studies have only focused on the composite action between steel tube and concrete and dampers itself, ignoring the influence of other structural components such as the gusset plate in the connection.

The aim of this research is to investigate the cyclic performance of beam-to-CFT connection with gusset plates by experimental and numerical simulations to study its failure modes, hysteresis characteristics, ductility, and energy dissipation. These connections are designed to reduce concentration of stresses at the steel connection near the weld around the CFT column, to help the force transfer between the beam and the column to be more smoothly, and to improve the overall ductility of these connections. In this research, representative tests have been carried out to study the seismic performance of connections.

2. Test Program

2.1. Test Specimens and Experimental Test Setup. Five test specimens were designed in the research by using the same type of hot-rolled beams ($HM194 \times 150 \times 6 \times 9$ and steel grade Q235) connected to medium-high round steel tubes ($d = 273$, $t = 8$, and steel Q235). The bending moment in the connection area is formed by applying vertical loads to the beam tip by using an MTS hydraulic loading jack. The section size of the beam and column corresponds to the full-size member in the frame structure, and the criterion of the strong column with the weak beam was considered in the design. The ends of the beam and column in the test device correspond to the inflection point of the deformation curves of actual structural members, which can be simulated by setting the pin boundary condition at both ends of the test members. In order to prevent the unexpected out-of-plane deformation of the specimens, transverse braces were installed near the top and bottom beam flange.

The details of the five specimens are illustrated in Figures 1 and 2, and the configuration information is summarized in Table 1. The specimen SJ-1 was used to assess the performance of connection without the gusset plate and set as the control group, in which the beam web directly penetrated through the CFT column and the root fillet weld at beam was located on both sides of the top and bottom flanges. Specimen SJ-2 was designed on the basis of the specimen SJ-1, but two extra gusset plates were welded to the beam flange and column wall through double-side fillet welds, aiming at investigating the influence of gusset plates. For specimen SJ-3, a gusset plate was penetrated through the CFT column and inserted to the beam slot by fillet welds, and the root of slotted beam flange was connected to the column wall like the specimen SJ-1, the beam web, and the gusset plate was connected by butt welds. For specimen SJ-4, the fillet weld between the beam flange and column face was removed. The gap between the beam flange and column wall was 20 mm in SJ-5 according to SJ-4. The connection zone of the five specimens was all attached with strain gauges, and the position of the strain gauges was basically the same as that of the specimen SJ-3, and several locations of the specimens were cleaned and dried to prepare for the installation of strain gauges, as illustrated in Figure 3.

Generally, the section size was controlled by the ultimate capacity of the MTS loading system. During the cyclic loading until 0.01 rad, the specimens were designed to stay in relatively elastic stage. Q235B steel was used in steel beams, columns, and gusset plates. Test samples for testing the material properties of steel were obtained from the same groups of plates and tubes as specimens'. The coupon test results are summarized in Table 2.

2.2. Instrumentation. As shown in Figure 4, the MTS loading device was mounted between the reaction steel frame and the beam tip and consisted of a 500 kN hydraulic actuator with a 200 mm equal stroke for both upward and downward directions. The displacement (δ_1) was measured by both a built-in displacement transducer of the hydraulic actuator and an external LVDT (linear variable differential transformer) named No.1, and the beam rotation (θ_b) was represented by δ_1/l_b . Two displacement transducers (Nos. 2 and 3) were installed to measure the column rotation according to the layout in Figure 5.

2.3. Test Procedure. The beam-column connection specimens were tested under the cyclic loading sequence recommended by ANSI/AISC-341-16 [11]. The loading procedure consisted of ten stages. The displacement and the number of cycles at each stage are shown in Figure 6. The displacement of the first three stages is 0.375%, 0.5%, and 0.75% of story drift, for 6 cycles in each stage. The rest of seven loading stages started with 1% of story drift, two cycles for each stage. The successive drift was increased by 0.5% from stage 4 to stage 6 and by 1% from stage 6 to stage 10. A quasi-static loading was applied in a displacement-controlled mode in a relatively low rate to record the deformation of the whole process during the specimens subjected to load cycles.

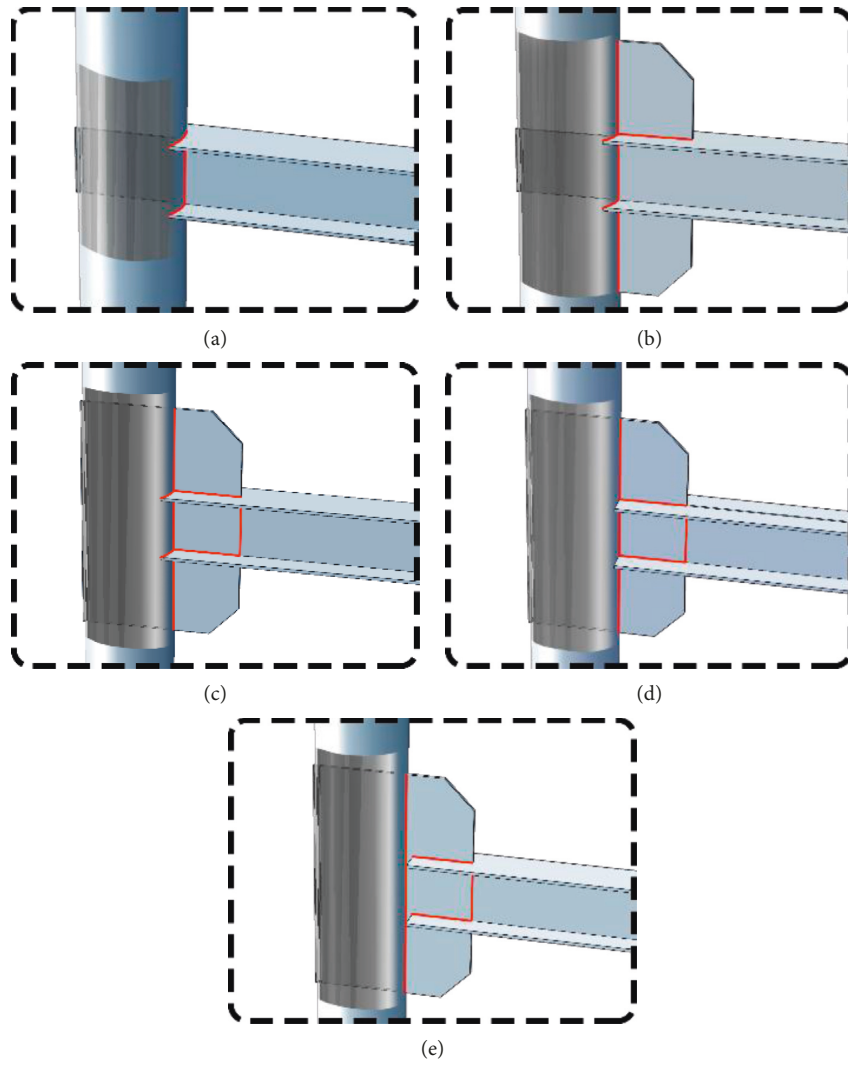


FIGURE 1: Graphic models of the five specimens. (a) Specimen SP-1. (b) Specimen SP-2. (c) Specimen SP-3. (d) Specimen SP-4. (e) Specimen SP-5.

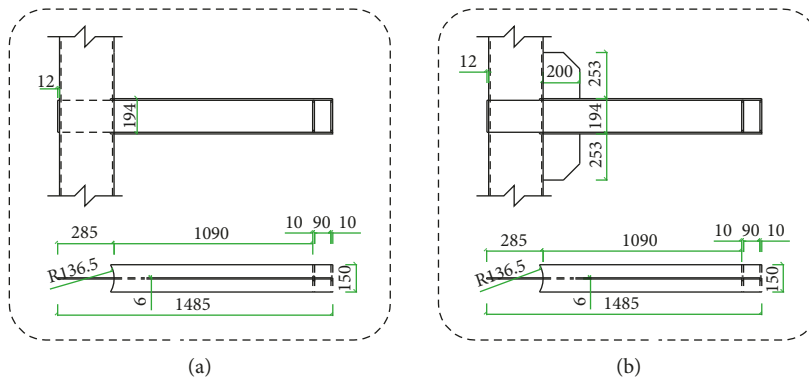


FIGURE 2: Continued.

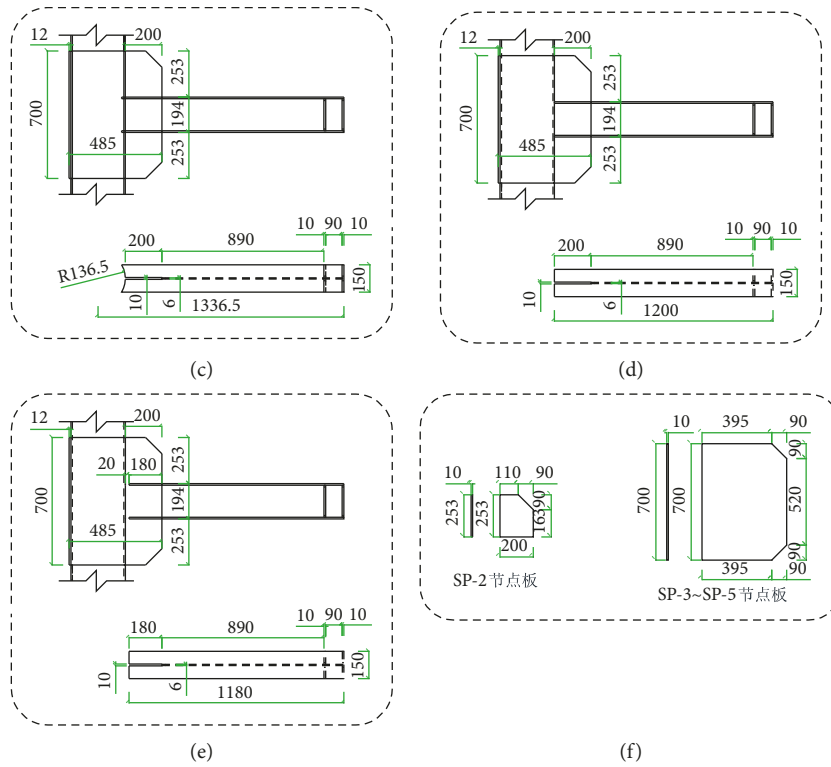


FIGURE 2: Connection details of the five specimens. (a) Specimen SP-1. (b) Specimen SP-2. (c) Specimen SP-3. (d) Specimen SP-4. (e) Specimen SP-5. (f) Configuration of the gusset plate.

TABLE 1: Geometric detail of specimens.

Specimen	Gusset plate	Penetration	The weld between the beam flange and CFT	Weld length between beam flange and gusset plate
SJ-1	×	Beam web	Weld	—
SJ-2	√	Beam web	Weld	200 mm
SJ-3	√	Gusset plate	Weld	200 mm
SJ-4	√	Gusset plate	—	200 mm
SJ-5	√	Gusset plate	—	180 mm

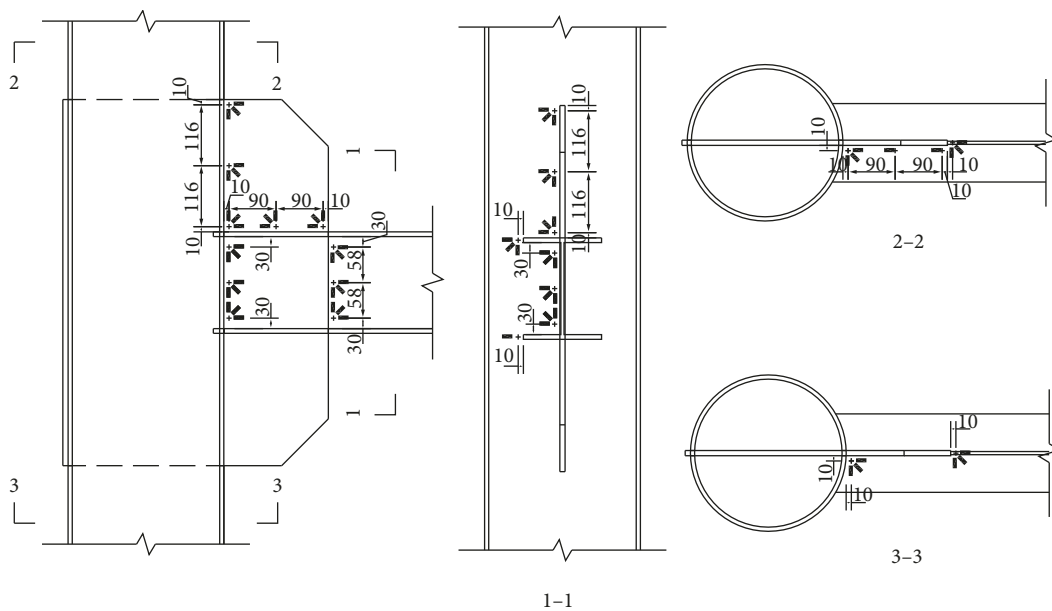


FIGURE 3: Layout of strain gauges distribution.

TABLE 2: Material properties of steel.

Material	Thickness (mm)	f_y (MPa)	f_u (MPa)	E (GPa)	Elongation (%)
Beam web	5.35	313.8	463.8	195.7	30.5
Beam flange	9.28	281.8	443.2	195.9	37.4
Gusset plate	9.31	275.1	443.3	191.1	39.4
Steel tube	6.91	297.4	463.5	190.5	33.1

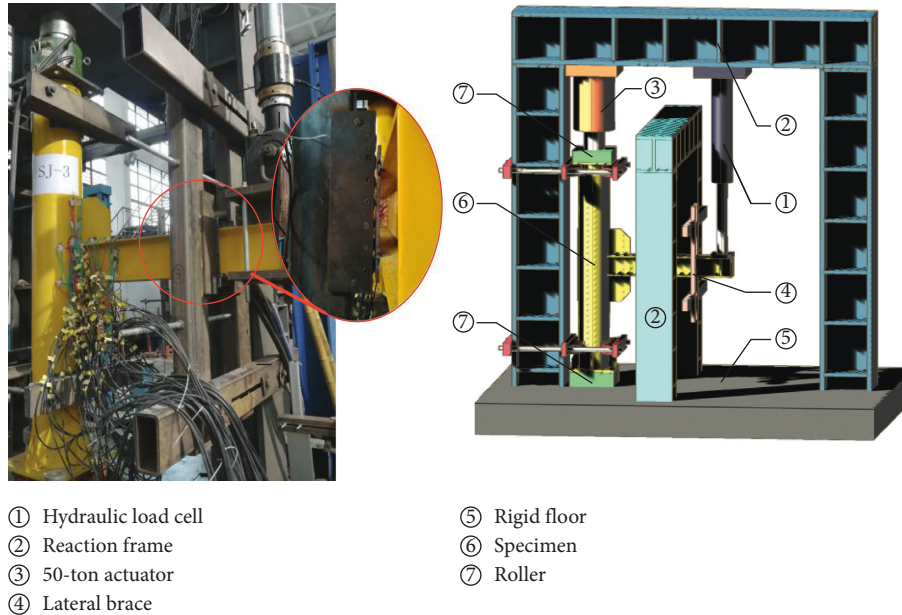


FIGURE 4: Experiment setup.

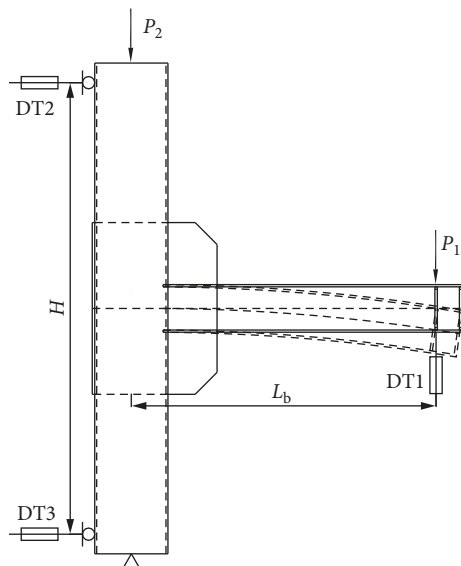


FIGURE 5: Layout of the displacement indicator.

3. Test Observation

3.1. Failure Modes

3.1.1. *Specimen SJ-1.* The flexural yield of the beam first appears at the beam flange in the first cycle of the 1% story drift angle; when the rotation reached 1.5% story drift angle,

there was a further yielding occurring in the beam flange. It can also be observed that a slight flaking of yellow paint in the beam flange near the beam end. During the last cycles of 1.5% story drift angle, some visible microcracks were initiated inside the fillet weld between the beam flange and column wall. As load increased, the paint of outer surface of the beam flange was completely peeled off during the last cycles of 2% story drift angle of the test, and the low-cycle fatigue crack became more extensive. The test on SJ-1 was terminated at the first cycle of 4% story drift angle due to complete crack in fillet welds and extension to the column web. At the end of the test, there was no obvious local buckling at the beam flange or web. The test specimen during the 4% story drift angle is depicted in Figure 7(a).

3.1.2. *Specimen SJ-2.* Before the first cycle of stage 4, specimen SJ-2 remained elastic, and the yellow paint at the outer surface of the beam flange near the exterior edge of the gusset plate flaked slightly. During the 3% and 4% story drift cycles, it can be observed that initial buckling was spread in the beam flange, as seen in Figure 7(b). When the cycles of 4% to 5% story drift angle were reached, the local buckling of the upper and lower beam flanges appeared and the beam web also started buckling. Thereafter, a minor crack occurred in the fillet weld between the gusset plate and beam flange. When the load cycles reached the end of 0.06 rad, there was a large local buckling appearing at the beam

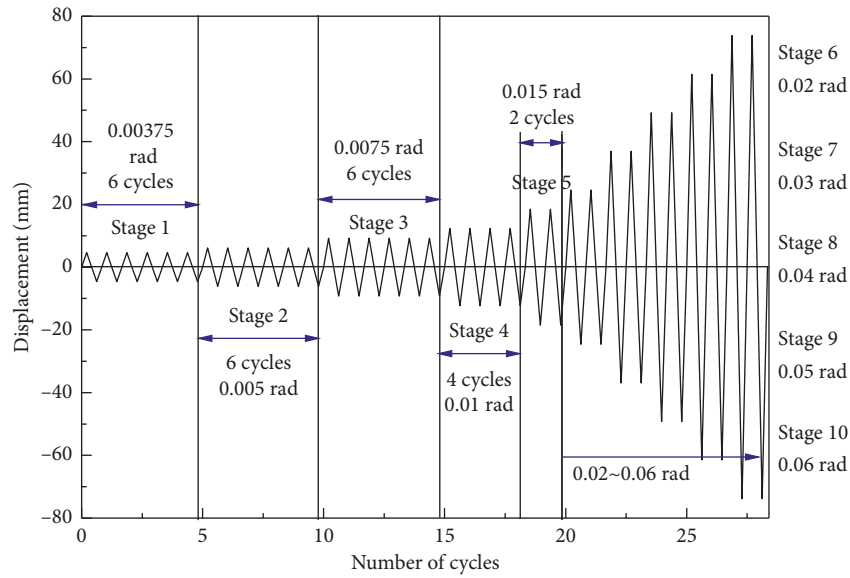


FIGURE 6: Loading procedure.

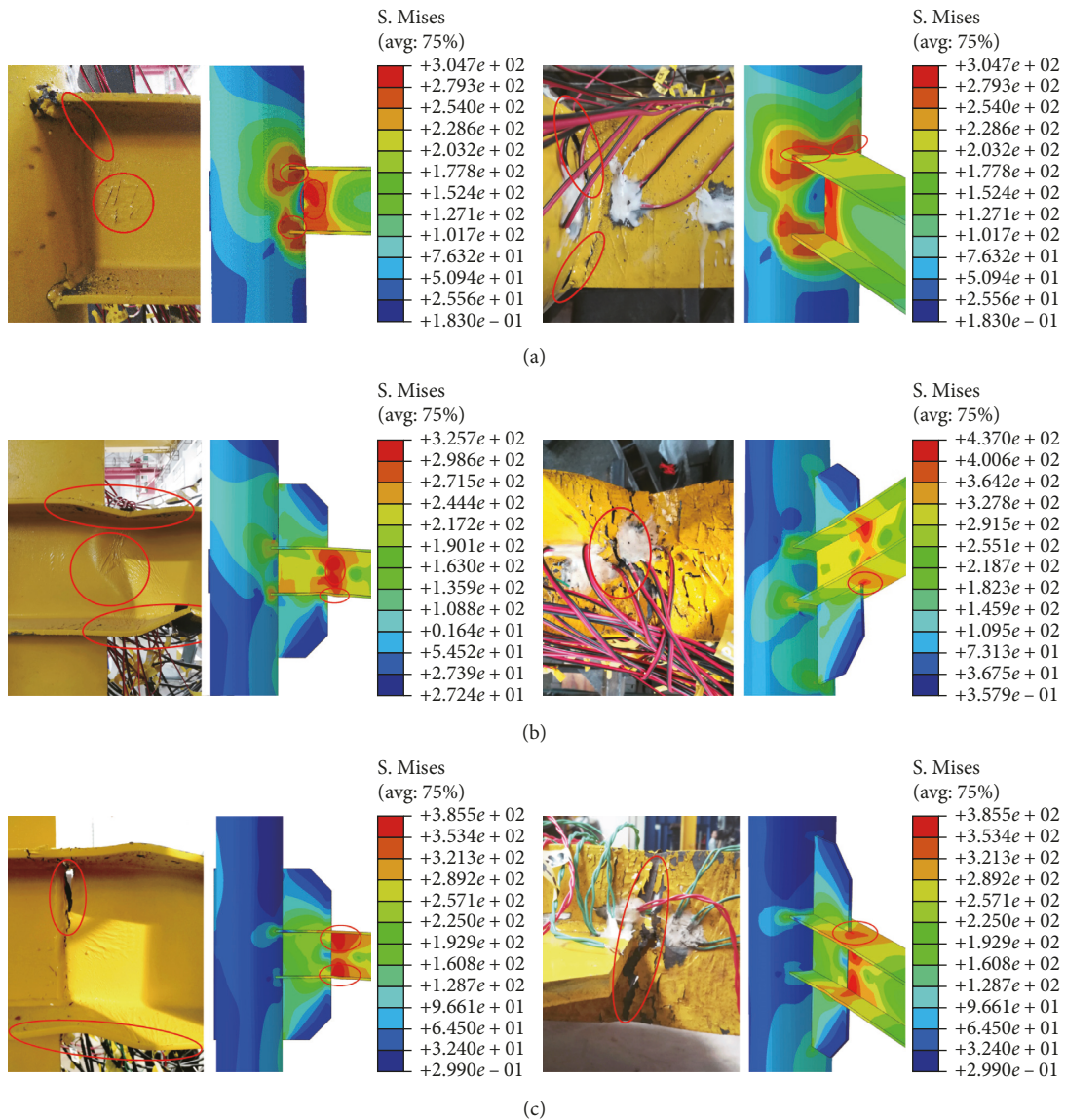


FIGURE 7: Continued.

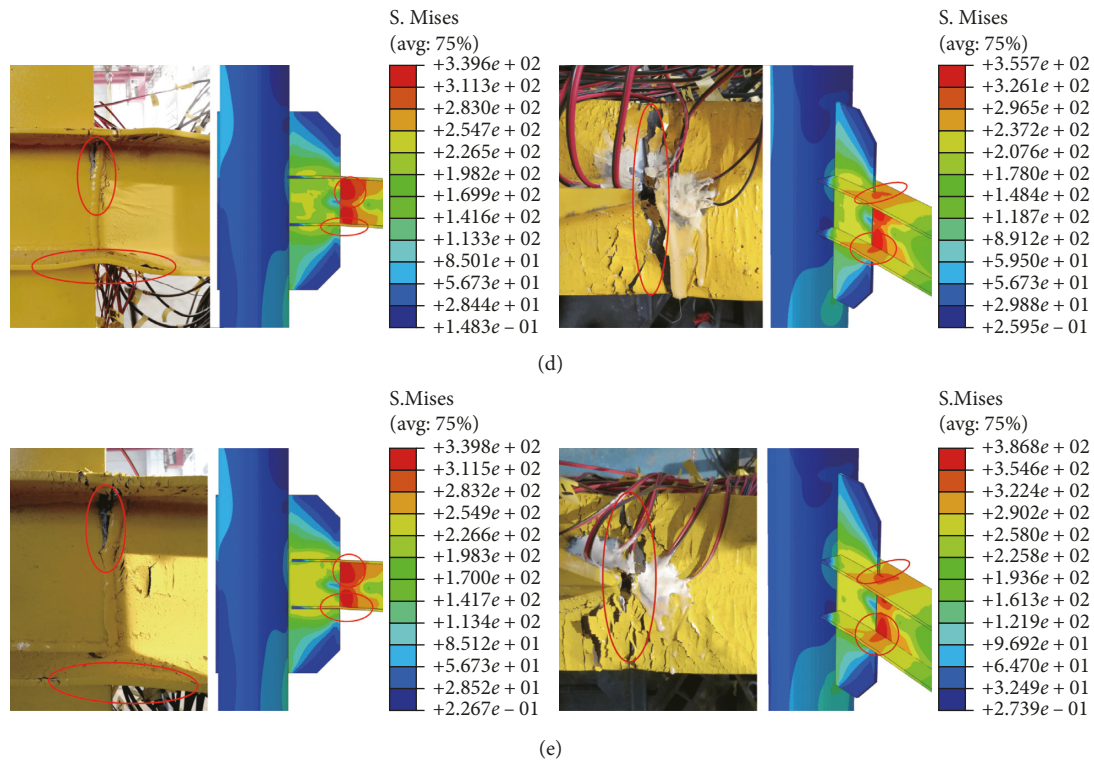


FIGURE 7: Loading procedure. (a) Failure mode of specimen SJ-1: experiment and FEM analysis. (b) Failure mode of specimen SJ-2: experiment and FEM analysis. (c) Failure mode of specimen SJ-3: experiment and FEM analysis. (d) Failure mode of specimen SJ-4: experiment and FEM analysis. (e) Failure mode of specimen SJ-5: experiment and FEM analysis.

compression flange. Finally, the test was terminated during the cycles of 6% story drift angle due to the sudden fracture of the beam flange or the failure of welds due to excessive deformations, along with the crack in the fillet weld spreading to the beam end. Figure 7(b) depicts specimen SJ-2 at 6% story drift angle.

3.1.3. Specimens SJ-3, SJ-4, and SJ-5. The behavior of the last three specimens was similar, first yielding appeared in the beam flange, followed by paints flaking. A slight buckling was found in the beam flange during the cycles of 3% story drift. With the cycles to 4% story drift, severe buckling with large displacement could be seen at the beam flange, and a microcrack was initially at the beam flange near the gusset plate, as shown in Figures 7(c)–7(e). Finally, the specimens failed by a transfixion fracture in the beam flange and beam web at the story drifts of 5%.

3.2. Strain Reading. As shown in Figure 8, the letter C means strain reading in the CFT column along the column height, and the letter P represents the strain reading in the gusset plate and beam web along the vertical direction of specimens. Beyond that, the different vertical loads at the beam end are expressed in the numbers contained in C-30 and P-60. The outer surface of the tension beam flange is set as the coordinate axis origin. Obviously, the value of the strain gauge at the tension zone of the column would be positive.

For better comparison, the strain reading would be multiplied by negative one.

Figure 8(a) illustrated that an earlier yield occurred in the steel tube around the weld of the beam web through the connection. No yielding was found in SJ-2 when the applied load was 65 kN. When the beam end loads were 100 kN, both the steel tube and the web enter the yield in SJ-2, and the stress on the steel tube is greater than that on the gusset plate. However, both SJ-3 and SJ-4 did not yield, which indicates that the penetrable gusset plate can relieve the stress concentration in the connection between the column and the beam, but the beam web is yielding in SJ-5 due to the shorter weld length between the beam flange and gusset plate.

4. Discussion of Test Results

4.1. Moment-Rotation Curves. In order to better analyze the data collected in the experiments from different specimens, the definition of the yield moment (M_y), the maximum moment (M_u), and the ultimate moment (M_f) are illustrated in Figure 9, and M_f is the bending moment corresponding to the reduction of the bending moment resistance of the connection to $0.85M_u$. The hysteretic curves of the specimens represented by the moment at column face versus story drift angle were obtained by dividing the total load cell displacement by the distance from the center of the load cell to the column centreline, as illustrated in Figure 10. Until the story drift angle reached 4%, the test specimens with the

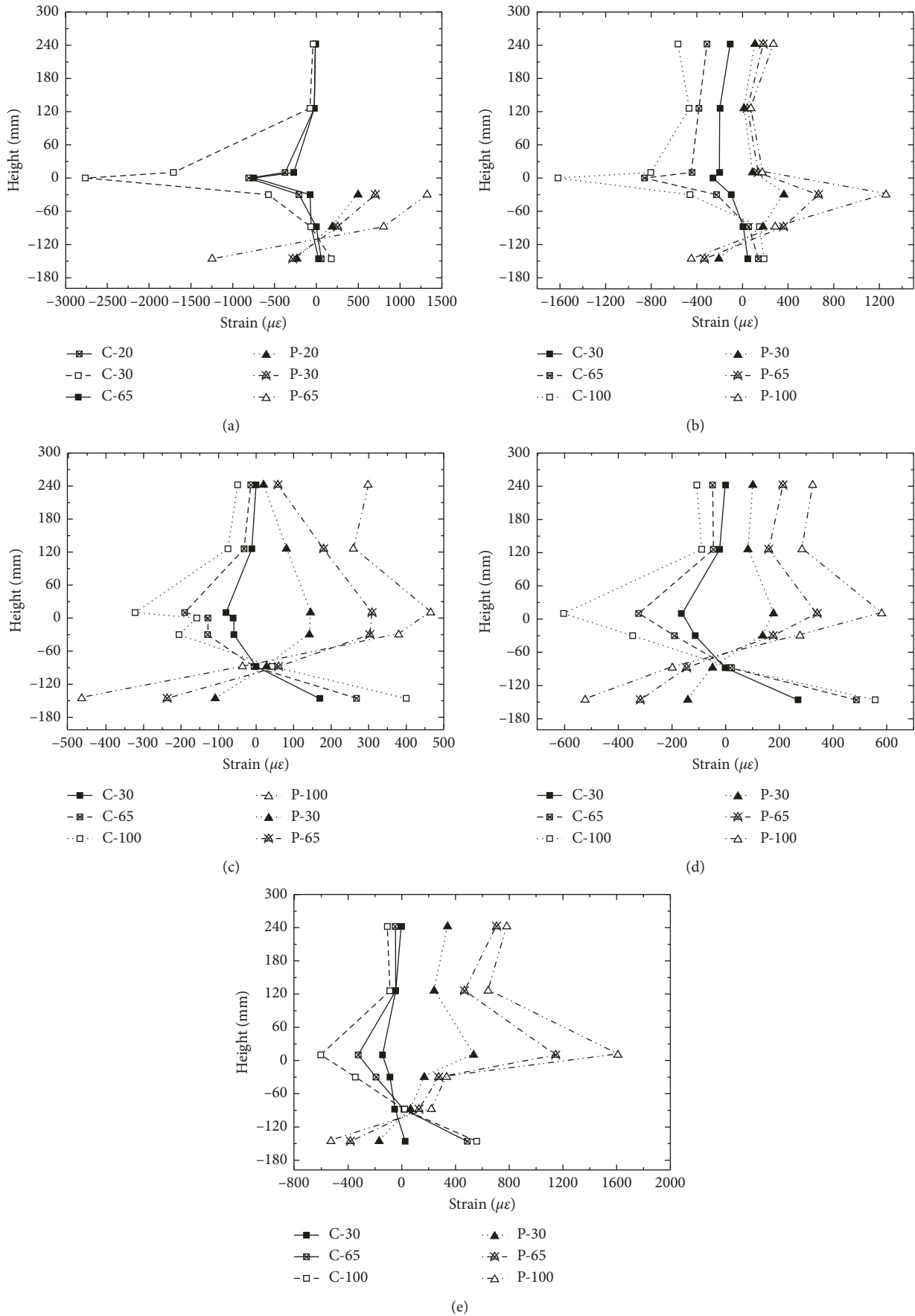


FIGURE 8: Key parameters in the moment-rotation relationship of specimens. (a) SJ-1. (b) SJ-2. (c) SJ-3. (d) SJ-4. (e) SJ-5.

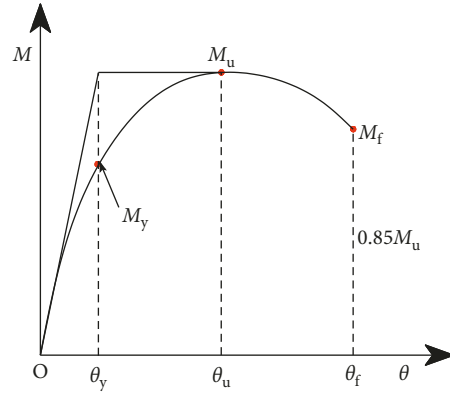


FIGURE 9: Key parameters in the moment-rotation relationship of specimens.

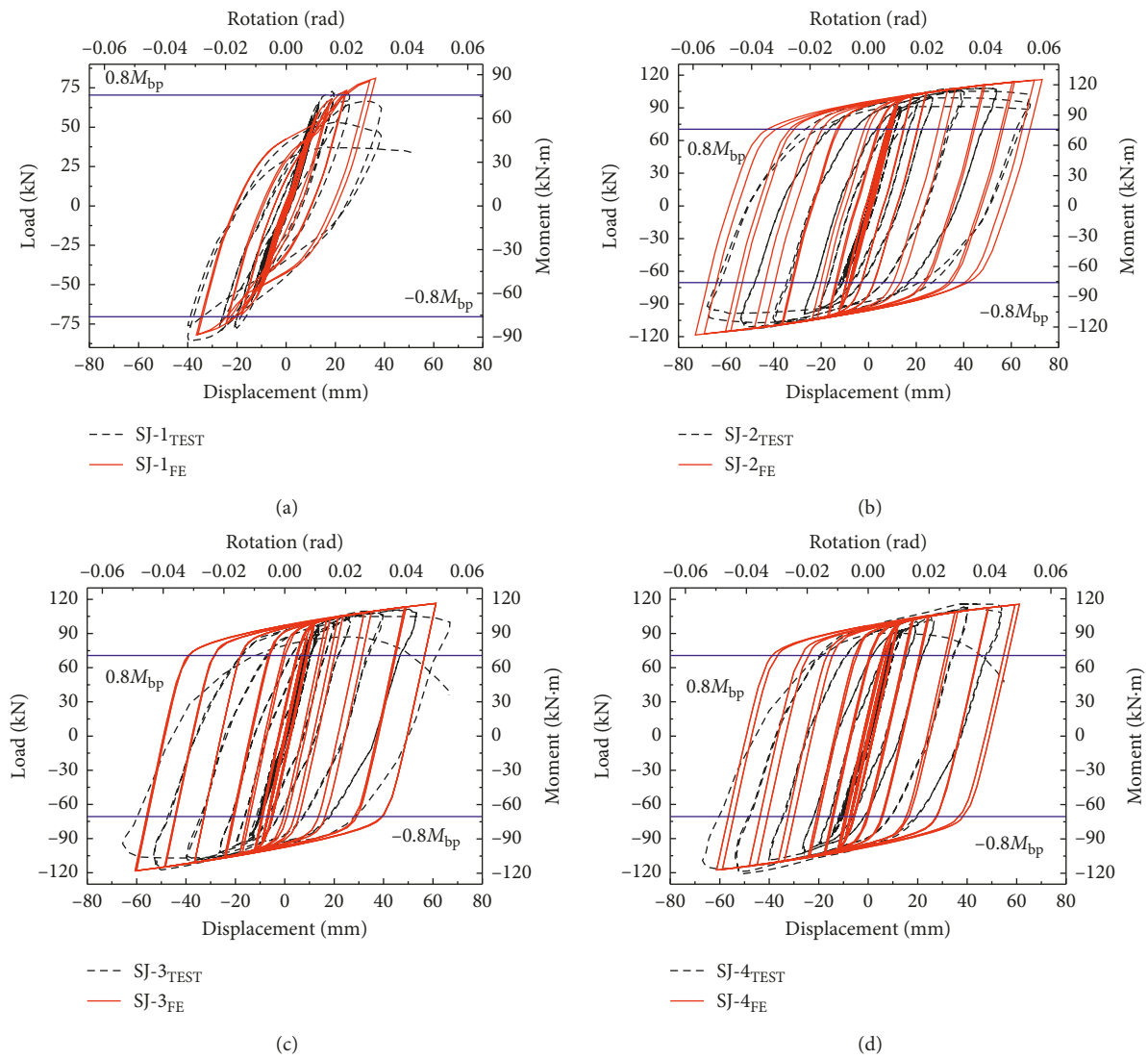


FIGURE 10: Continued.

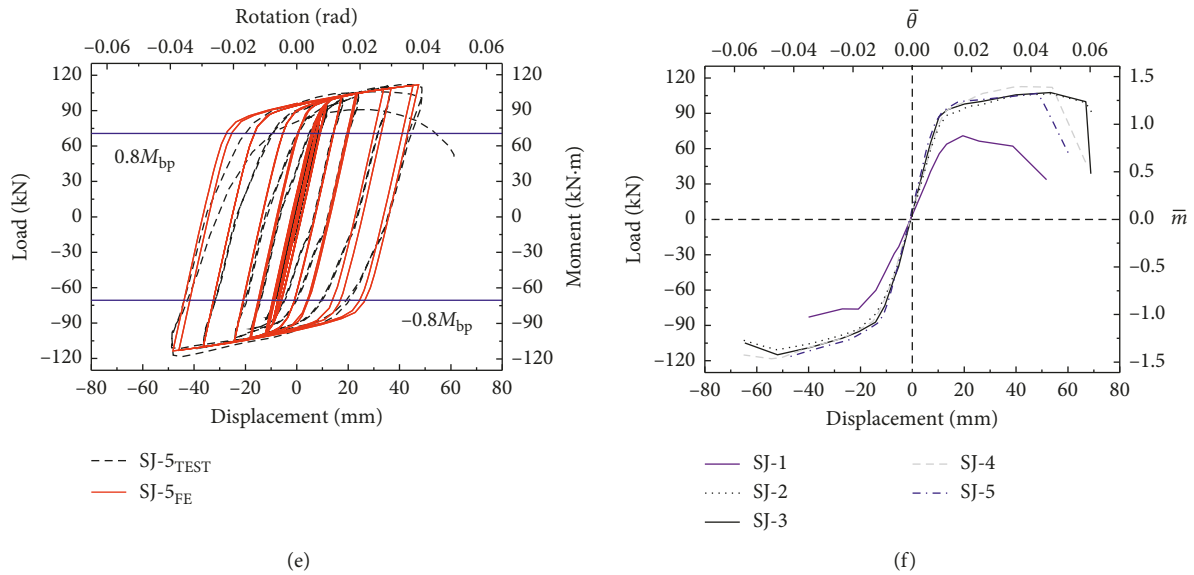


FIGURE 10: Hysterical and skeleton curves. (a) SJ-1. (b) SJ-2. (c) SJ-3. (d) SJ-4. (e) SJ-5. (f) Skeleton curves.

gusset plate exhibited stable and reliable hysteresis behavior with only small strength degradation.

The specification ANSI/AISC-341-16 [11] suggests that the composite special moment frame proposes a requirement that story drift angle should not be less than 0.04 rad.

In addition, the calculated flexural moment resistance of connection determined at column face should equal at least 0.8 nominal plastic moment resistance (M_{bp}) of the beam at story drift angle of 0.04 rad in the composite special moment frame. The story drift angles of specimens at different stages are summarized in Table 3. Specimens SJ-2 and SJ-3 achieved a total story drift for at least 0.05 rad with maximum 15% strength degradation, while SJ-4 and SJ-5 achieved at least 0.04 total story drift. Therefore, all the gusset plate connections meet the requirements of the ANSI/AISC-341-16 [11] which accepts maximum 20% strength degradation until 0.04 rad story drifts for qualifying a connection for special moment resisting frames.

As illustrated in Figure 11, the bending moment at the location of the plastic hinge revealed that the connection with gusset plates had bearing moment that was 1.18 to 1.25 times larger than M_{bp} in the gusset plate connection, respectively. Considering the strain hardening effect, the bending moment at the plastic hinge of specimens should be larger than the theoretical value M_{bp} . The specification ANSI/AISC-341-16 [11] suggests an overstrength factor of $1.1R_y = 1.21$ to calculate the actual bending moment considering the strain hardening phenomenon. As previously discussed, this method can closely estimate the ultimate bending moment at the plastic hinge. And, the experimental results of bending moment at the plastic hinge is close to the method suggested by ANSI/AISC-341-16 [11]; therefore, it can be applied in the practical design of this type of connections.

4.2. Connection Rigidity. As suggested by CEN-1993-1-8 [24], the connection rigidity and strength can be classified based on their characteristic of their moment-rotation curves; on the perspective of connection rigidity, a joint can be evaluated as nominally pinned, rigid, or semirigid by its initial rotational stiffness ($S_{j,ini}$) according to the boundaries suggested by EC3 part 1.8: a joint is nominally pinned if $S_{j,ini} \geq 00.5EI/L$, where E , I , and L are elasticity modulus, second moment of area, and the length of the steel beam, respectively. A rigid joint satisfies $S_{j,ini} \geq k_b EI/L$, $k_b = 25EI/L$ for nonbraced frame and $k_b = 8EI/L$ for braced frame. In terms of strength, the minimum required connection resistance for partial-strength design is $0.25M_{bp}$ and the full-strength connection resistance is beyond M_{bp} . Two parameters are introduced to, respectively, normalize the moment and rotation of the connection to facilitate analysis and comparison of data collected in the experiments. The definition of the two parameters is as follows:

$$\bar{m} = \frac{M}{M_{bp}}, \quad (1)$$

$$\bar{\theta} = \frac{\theta}{M_{bp}} \frac{EI_b}{L_b}.$$

For the aforementioned connection classified method, the analysis results of test joint connection with different types are shown in Figures 10 and 12. It indicates that the test joints with the gusset plate could be regarded as a rigid and full-strength connection in the braced frame; it also could be considered as semirigid with a full-strength connection in the nonbraced frame.

4.3. Ductility. The ductility of specimens is defined as the ability of elastic-plastic deformation of specimens without obvious reduction of bearing capacity. In order to define

TABLE 3: Moment and rotation at different stages.

Specimen number	θ_y (mm)	M_y (kN)	θ_{max} (mm)	M_{max} (kN)	θ_u (mm)	M_u (kN)
SJ-1	0.011	46.79	0.021	84.63	0.032	71.94
SJ-2	0.010	70.46	0.043	119.71	0.056	101.76
SJ-3	0.009	71.05	0.042	122.39	0.054	104.03
SJ-4	0.010	74.47	0.043	127.41	0.046	108.30
SJ-5	0.009	70.64	0.039	123.52	0.042	104.99

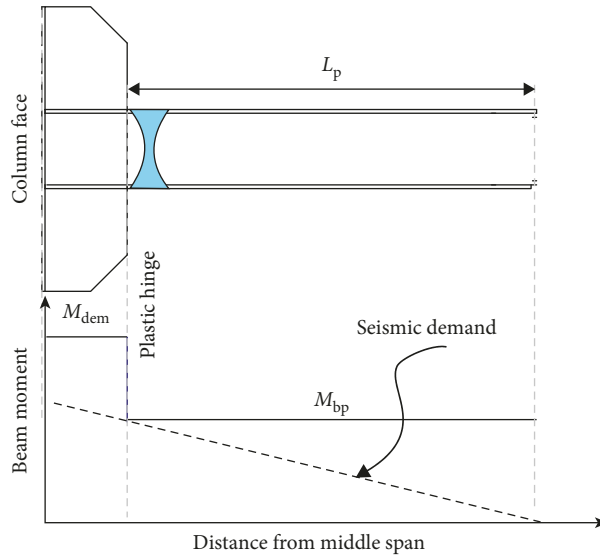


FIGURE 11: Bending moment diagram of the connection.

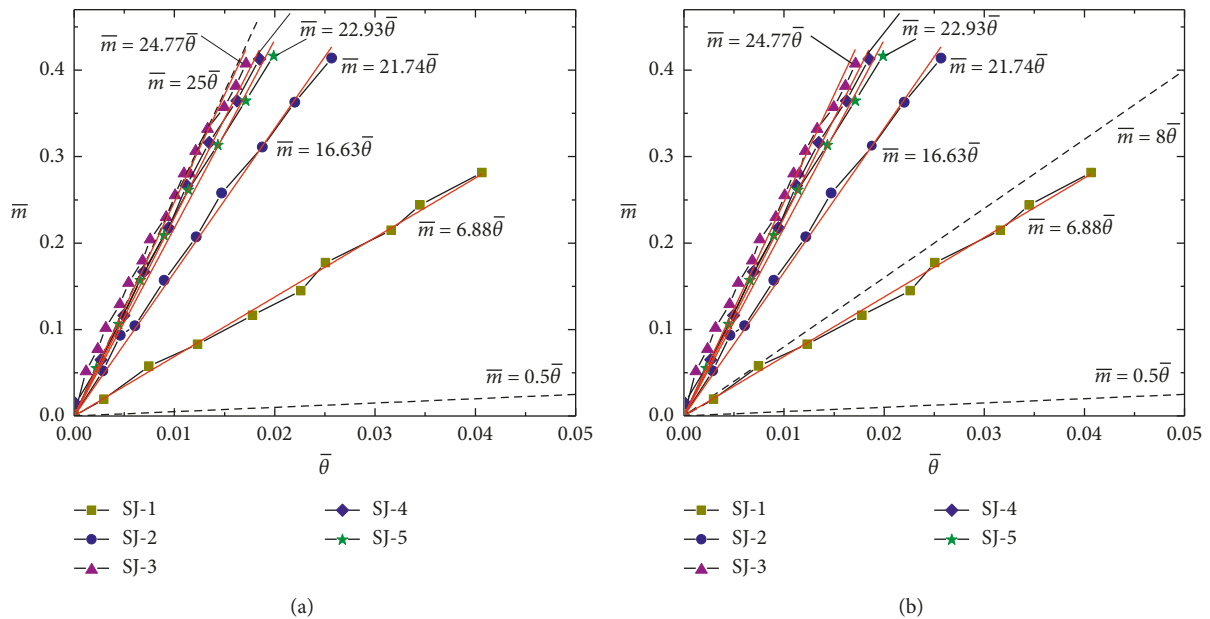


FIGURE 12: Connection classification by initial stiffness. (a) Nonbracing frame. (b) Bracing frame.

the ductility of the joint in this study, the ductility ratio (μ) is calculated by equation (2), where θ_y is the story drift angle when joint yielding θ_u is the story drift angle corresponding to the bending moment resistance of the connection reduced to $0.85M_{max}$. Although this

evaluation method may underestimate the ductility of the connection to a certain extent, it is still reliable and effective to compare the ductility among specimens. The comparison of the ductility ratios is summarized in Table 4.

TABLE 4: Ductility factor of specimens.

Specimen number	$\theta_e/[\theta_e]$	$\theta_p/[\theta_p]$	μ
SJ-1	2.75	1.05	2.91
SJ-2	2.50	2.30	5.60
SJ-3	2.25	2.25	6.00
SJ-4	2.50	1.80	4.60
SJ-5	2.25	1.65	4.67

$$\mu = \frac{\theta_u}{\theta_y} \quad (2)$$

Ultrasonic testing was used to test the quality of the weld in the connection area before the test, and the quality of the weld is not fully guaranteed, for defects are inevitable in the welds, which leads to brittleness of joints. Nonductile cracking or tearing affects the ductility of joint, which further affects the seismic performance of specimens. Another important point worth noting is that weld failure was found in SJ-1 with a lowest ductility ratio ($\mu = 2.91$) due to the fillet welds applied between the beam flange and column wall instead of using complete joint penetration groove welds. The ductility ratio of specimens with the gusset plate (SJ-2 and SJ-3) has greatest ductility ratios, as a result of additional force transferring path provided by the gusset plate. All the shear force and moment in specimens SJ-4 and SJ-5 were transferred by the gusset plate alone; consequently, stress concentration would be more serious that led to premature fracture around welds and weak cross section.

According to the Chinese Building Seismic Design Code GB50011-2010 [25], which specifies the elastic story drift angle limit value $[\theta_e]$ and the elastic-plastic interlayer story drift angle limit value $[\theta_p]$ in the multilayer and high-steel structures are $[\theta_e] = 1/250$ and $[\theta_p] = 1/50$. As can be seen from the results in Table 4, almost all of the test specimens meet the requirements for deformation checks under seismic loading.

4.4. Energy Dissipation. The energy absorption (dissipation) capability is one of the key points to evaluate the seismic performance of a structure, and the total energy dissipation capacity is defined as the envelope area of the hysteretic curve, which indicates the energy dissipation capacity. Equivalent viscous damping (EVD) is one of the three key parameters evaluating the energy dissipation capacity of connection components. The method to calculate EVD is defined in Figure 13(a). In equation(3), S_{ABC} and S_{CDA} refer to the upper half and lower half areas of the hysteresis curve, respectively. S_{OBE} and S_{ODF} represent corresponding triangular areas:

$$h_e = \frac{1}{2\pi} \frac{S_{ABC} + S_{CDA}}{S_{OBE} + S_{ODF}} \quad (3)$$

Figure 13(c) describes the changes of EVDs of the four specimens with increasing story drift angle; at the drift level of 0.04 rad, the values of EVD for all tested specimens with the gusset plate were above 0.4, which indicates good energy dissipation capacity of all specimens.

Another two properties are the energy dissipated in each step (E_i) and accumulated energy dissipation (E_t). Figures 13(b)–13(d) show E_i and E_t of the five specimens; the accumulated energy dissipations of the specimens with the gusset plate at failure varied between 50 kJ and 70 kJ. For the three specimens with penetrated gusset plate show similar responses at ultimate state; E_t of specimen with the gusset plate at 0.03 rad was almost twice that of specimen SJ-1; therefore, the presence of the gusset plate could largely enhance energy dissipation behavior. However, in comparison with SJ-3 and SJ-4, the increase caused by weld between the column and beam flange was not obvious. It is worth noting that the overall performance of specimen SJ-2 possessed the largest accumulated energy dissipations.

5. Finite Element Analysis

5.1. General. A finite element method (FEM) analysis model was established in ABAQUS to simulate specimens without gusset plate (SJ-1) and specimens with gusset plate (SJ-2, SJ-3, SJ-4, and SJ-5). The FEM results were verified by the experimental dates. Further parametric analyses were conducted and accordingly some design suggestions were presented.

5.2. Material Modeling of Steel and Concrete. The yield strength (f_y) and the ultimate strength (f_u) of steel were adopted for every actual tensile coupon test result, as summarized earlier in Table 1. Poisson's ratio was assumed to be 0.3. The constitutive relationship of steel adopts the three-fold line model. In general, the concrete material can use the damage plastic model, but the damage plasticity model is not applicable to the CFT column. In order to consider the concrete restraint effect in CFT, the peak strain and transformation will be increased according to Han et al. [26]. The input stress-strain branch of the strain curve was modified, as shown in Figure 14.

5.3. Assessments of the Finite Element Models. In Figure 15, steel tubes, beam flanges, beam webs, gussets, and concrete were all meshed using 8-node linear brick incompatible mode components (C3D8I), which reduced integration and uses hourglass control, and structured mesh controls were used for all components. The general mesh size for the entire model is 13 mm, and there were at least three layers in the thickness direction. According to the previous study [9, 27], by using this mesh size for numerical analysis, better calculation results can be obtained with lower computational cost. Surface-surface contact interaction was applied to simulate the interaction between steel and reinforced concrete by specifying the normal hard contact and tangential friction (with a friction coefficient of 0.6, in Coulomb friction model, maximum surface bond stress is 0.6 MPa). The interaction caused the concrete to separate from the steel tube after partial buckling of the steel tube, and the merge characteristics are used to simulate the interaction between the steel tube, the beam, and the gusset. The boundary conditions are completely similar to the actual

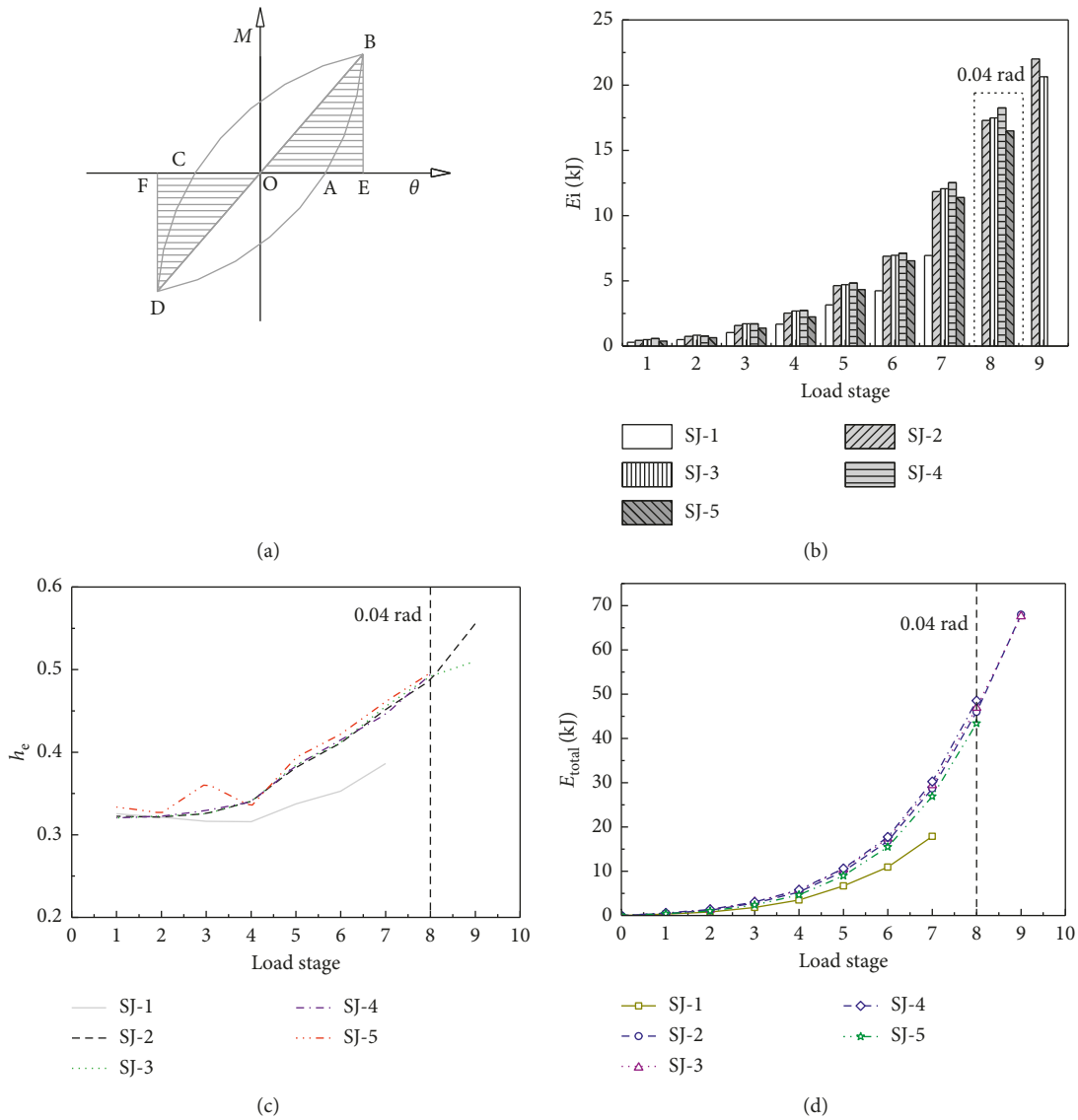


FIGURE 13: Comparison of energy dissipation and the hysteretic loop in the test specimens. (a) Definition of a hysteretic loop. (b) Energy dissipated during each step. (c) Equivalent viscous damping. (d) Accumulated energy dissipation.

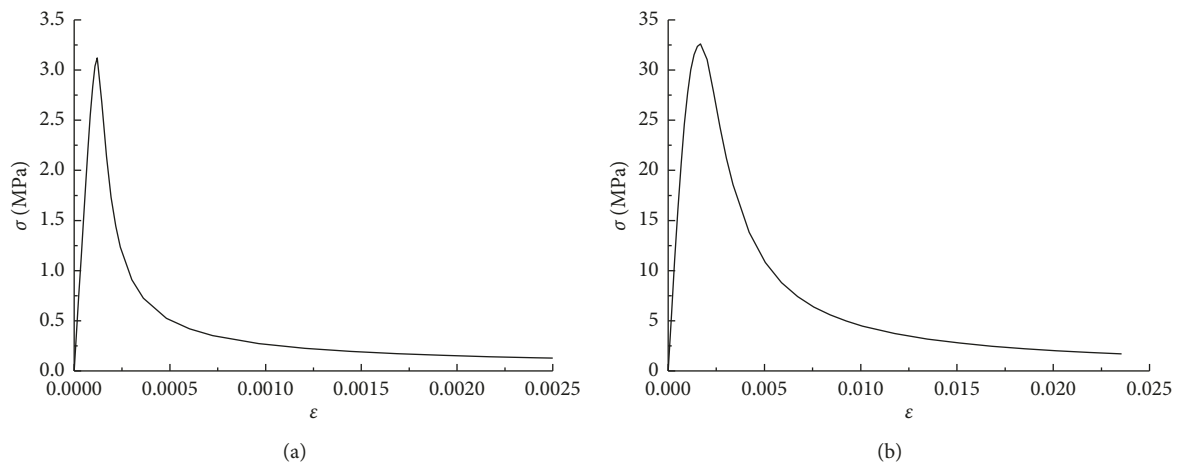


FIGURE 14: Stress-strain curves of the filled concrete in the simulation. The behavior for filled concrete in tension (a) and in compression (b).

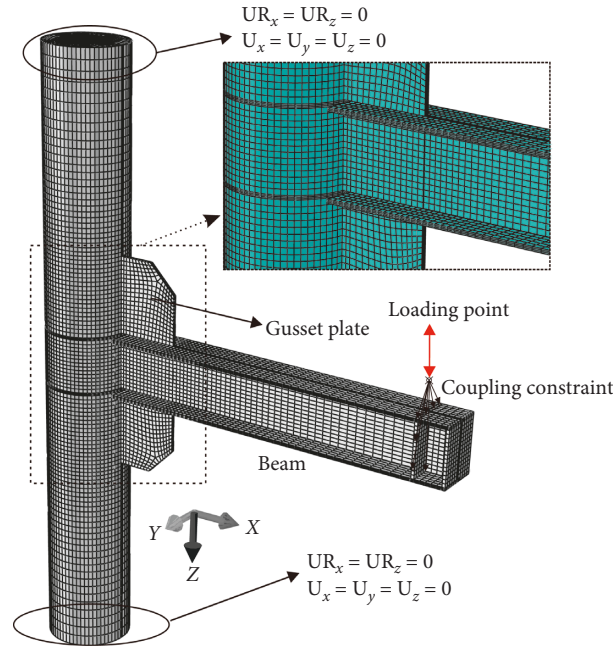


FIGURE 15: Finite element model and mesh.

boundary conditions of the specimen. In order to simulate the hinge constraint of the column end and the beam end, coupling constraints are generated at the end of the column and the beam to eliminate unrealistic stress and strain concentration. By limiting the out-of-plane motion of the upper and lower flanges of the beam to prevent overall instability, lateral constraint was provided at the beam flange at certain area during testing.

5.4. Comparison of Tests and Numerical Analysis. Table 5 presents the FE analysis results in comparison with the test results, and the results of the FE analysis agree with the experimental behavior of the examined joints. Indeed, the plastic deformation mode identified during testing corresponds to the one observed in the FE model, and the response curves show good agreement in some ways of initial rotation stiffness (S_{ji}) and plastic moment (M_p) [27]. The strain and stress distributions for SJ-1, SJ-2, SJ-3, and SJ-4 are shown in Figure 10. Plastic hinges formed in the beam are observed in simulation results which coincide with the failure modes found in test results.

5.5. Weld Length. In order to investigate the influence of the welding length of the beam flange to the gusset plate, on the basis of SJ-5, the welding length was modified in the simulation, and the welding lengths were 190 mm, 180 mm, 170 mm, 160 mm, 140 mm, 120 mm, and 100 mm. The numerical models were numbered sequentially as SJ5-W1~SJ5-W7, and the specimen SJ5-W2 and the specimen SJ-5 were the same models.

As summarized in Table 6, it could be found that extending the welding length of the flange and the joint plate in a certain range would help to improve the ultimate bending moment and the initial rotational stiffness of joints.

TABLE 5: Validation between experiment and finite element analysis.

Specimens	Maximum displacement (mm)		Ultimate load (kN)		Initial stiffness $S_{j,ini}$ / (kN·m·rad ⁻¹)	
	FEM	Exp	FEM	Exp	FEM	Exp
SJ-1	36.9	38.6/ -39.9	80.2	72.8/-85.9	11963	12258
SJ-2	73.8	68.0/ -65.4	117.0	108.0/ -113.6	28181	29616
SJ-3	61.5	66.9/ -64.6	116.7	111.3/ -117.5	52062	44114
SJ-4	61.5	66.8/ -65.0	116.0	115.9/ -121.0	44021	40845
SJ-5	61.5	61.2/ -48.8	115.3	112.0/ -118.3	43081	38752

When the welding length of the beam flange and the joint plate reached the height of the section of the steel beam, the increase of the ultimate bending moment and initial stiffness is not obvious. Therefore, the welding length between the gusset plate and beam flange should not be less than the height of the connected beam.

5.6. Strengthen Pattern. In order to avoid or delay the fracture of the steel beam, on the basis of specimen SJ-5, the connection area was strengthened by welding cover plate and web plate; as illustrated in Figure 16, the strengthened model was named SJ5E. The specific size of the cover plate was 240 mm × 50 mm × 8 mm, and the web plate was 140 mm × 120 mm × 8 mm, and the ultimate failure modes and Mises stress distribution of the connections and beam end are presented in Figures 16 and 17. By comparing the stress distribution of experimental specimens and

TABLE 6: Percentage change of characteristic quantities of initial stiffness and plastic moment resistance with different weld lengths between the gusset plate and beam flange.

Specimens	$S_{j,ini}/(\text{kN}\cdot\text{m}\cdot\text{rad}^{-1})$	Percentage (%)	M_u (kN·m)	Percentage (%)	M_p (kN·m)	θ_p (rad)
SJ5-W1	43984	30.4	123.5	16.7	106.3	2.42×10^{-3}
SJ5-W2	43081	27.7	122.8	16.1	106.4	2.46×10^{-3}
SJ5-W3	42165	25.0	121.7	15.0	106.4	2.53×10^{-3}
SJ5-W4	41171	22.0	120.3	13.7	106.1	2.58×10^{-3}
SJ5-W5	38969	15.5	116.8	10.4	102.5	2.63×10^{-3}
SJ5-W6	36499	8.2	112.1	6.0	94.7	2.60×10^{-3}
SJ5-W7	33741	—	105.8	—	86.0	2.55×10^{-3}

Note. $S_{j,ini}$ is the initial rotational stiffness; M_u is the moment resistance at 0.05 rad; M_p refers to plastic moment resistance; θ_p rotation corresponds to M_p ; percentage means the increasing comparing to SJ-5-W7.

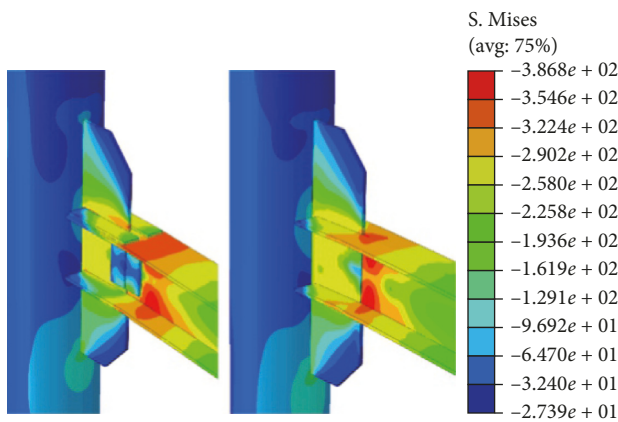


FIGURE 16: Stress nephograms of specimens SJ5 and SJ5E.

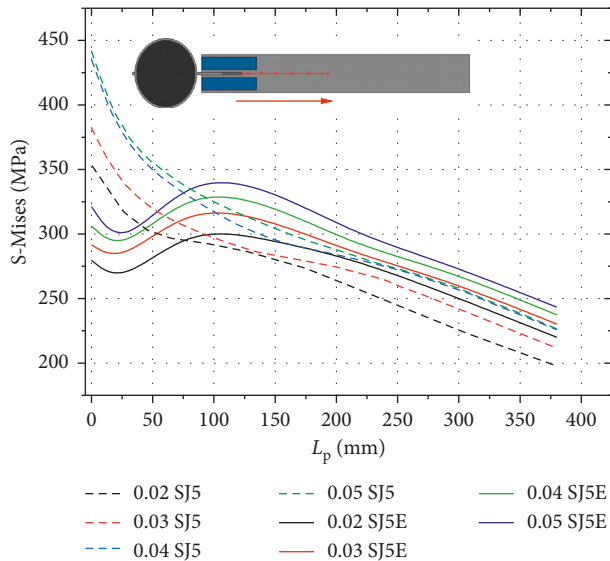


FIGURE 17: Stress path at beam end at different rotations.

strengthened models, the plastic hinge forming in the steel beam was moved to the edge of the cover plate and the web plate, away from the welding area of the steel beam and the joint plate, and the possibility of steel beam fracture at the weld may be reduced at the stress path of the beam end [28]. The initial rotational stiffness was significantly enhanced in strengthen models; meanwhile, the ultimate moment resistance was slightly improved.

6. Summary and Conclusion

This study involved an experiment to investigate the cyclic performance of the CFT column connection with penetrated gusset plate. The experiment and numerical analysis results presented herein support the following conclusions:

- (1) The connection with a penetrated gusset plate effectively reduced stress and strain concentration at the weld between the column and beam and largely moves the plastic hinges away from the column face. In addition, it could significantly improve the ductility and energy dissipation capacity of the connection under cyclic loading, achieving a plastic rotation at least 4% total story drift and a maximum strength reduction of 15%.
- (2) The connection without the gusset plate failed due to fracture at the fillet weld, and the penetrated beam web connection with additional gusset plate failed for an extreme plastic hinge in the beam. The fracture was found in the three penetrated gusset plate connections due to the slot and heat-affected zone in the beam with large plastic deformation in the beam.
- (3) The experimental results of bending moment at the plastic hinge is close to the method suggested by ANSI/AISC-360-16 which adopts an overstrength factor of $1.1R_y = 1.21$ to calculate the actual bending moment considered in the strain hardening phenomenon.
- (4) The welding length between the beam flange and penetrated gusset plate should not be less than the height of the connected beam. The specimen SJ-5 reinforced by additional cover plates and web plates will increase the stiffness and ultimate moment and properly enhance the ductility by moving the plastic hinge away from the slot and heat-affected zone of the beam.

Data Availability

The data used to support the findings of this study are available from the first author upon request.

Conflicts of Interest

The authors declare no conflicts of interest.

Acknowledgments

This study was supported by the National Natural Science Foundation of China (Grant nos. 51638009; 51778241; 51978279), the Fundamental Research Funds for the Central Universities (Grant nos. 2019MS121; 2019PY20; 2019ZD47), Chinese Postdoctoral Foundation of China (Grant no. 2019M652898), and the Young Innovative Talents Program in Universities and Colleges of Guangdong Province (Grant no. 2018KQNCX006).

References

- [1] H. Fan, Q. S. Li, A. Y. Tuan, and L. Xu, "Seismic analysis of the world's tallest building," *Journal of Constructional Steel Research*, vol. 65, no. 5, pp. 1206–1215, 2009.
- [2] K.-C. Tsai, P.-C. Hsiao, K.-J. Wang et al., "Pseudo-dynamic tests of a full-scale CFT/BRB frame—part I: specimen design, experiment and analysis," *Earthquake Engineering and Structural Dynamics*, vol. 37, no. 7, pp. 1081–1098, 2008.
- [3] L.-H. Han, W. Li, and R. Bjorhovde, "Developments and advanced applications of concrete-filled steel tubular (CFST) structures: members," *Journal of Constructional Steel Research*, vol. 100, no. 9, pp. 211–228, 2014.
- [4] Z. Lai and A. H. Varma, "Noncompact and slender circular CFT members: experimental database, analysis, and design," *Journal of Constructional Steel Research*, vol. 106, no. 10, pp. 220–233, 2015.
- [5] S. Xu, C. Wu, Z. Liu, and R. Shao, "Experimental investigation on the cyclic behaviors of ultra-high-performance steel fiber reinforced concrete filled thin-walled steel tubular columns," *Thin-Walled Structures*, vol. 140, pp. 1–20, 2019.
- [6] A. Elremaily and A. Azizinamini, "Experimental behavior of steel beam to CFT column connections," *Journal of Constructional Steel Research*, vol. 57, no. 10, pp. 1099–1119, 2001.
- [7] A. H. Varma, J. M. Ricles, R. Sause, and L.-W. Lu, "Seismic behavior and modeling of high-strength composite concrete-filled steel tube (CFT) beam-columns," *Journal of Constructional Steel Research*, vol. 58, no. 5–8, pp. 725–758, 2002.
- [8] C.-T. Cheng and L.-L. Chung, "Seismic performance of steel beams to concrete-filled steel tubular column connections," *Journal of Constructional Steel Research*, vol. 59, no. 3, pp. 405–426, 2003.
- [9] J. Pan, P. Wang, Y. Zheng, Z. Wang, and D. Liu, "An analytical study of square CFT columns in bracing connection subjected to axial loading," *Advances in Civil Engineering*, vol. 2018, Article ID 8618937, 15 pages, 2018.
- [10] CEN-1994-1-1, "Eurocode 4: design of composite steel and concrete structures," in *Part 1-1: General Rules and Rules for Buildings*, British Standards Institution, London, UK, 2004.
- [11] ANSI/AISC-341-16, *Seismic Provisions for Structural Steel Buildings*, American Institute of Steel Construction, Chicago, IL, USA, 2016.
- [12] Y. Kurobane, J. A. Packer, J. Wardenier, and N. Yeomans, *Design Guide for Structural Hollow Section Column Connections*, TÜV-Verlag GmbH, Köln, Germany, 2004.
- [13] Y. Qin, Z. Chen, and X. Wang, "Experimental investigation of new internal-diaphragm connections to CFT columns under cyclic loading," *Journal of Constructional Steel Research*, vol. 98, no. 7, pp. 35–44, 2014.
- [14] S. R. Mirghaderi, S. Torabian, and F. Keshavarzi, "I-beam to box-column connection by a vertical plate passing through the column," *Engineering Structures*, vol. 32, no. 8, pp. 2034–2048, 2010.
- [15] C.-H. Kang, K.-J. Shin, Y.-S. Oh, and T.-S. Moon, "Hysteresis behavior of CFT column to H-beam connections with external T-stiffeners and penetrated elements," *Engineering Structures*, vol. 23, no. 9, pp. 1194–1201, 2001.
- [16] X. Qin, W. Wang, Y. Chen, and Y. Bao, "Experimental study of through diaphragm connection types under a column removal scenario," *Journal of Constructional Steel Research*, vol. 112, pp. 293–304, 2015.
- [17] G. Macrae, C. W. Roeder, C. Gunderson, and Y. Kimura, "Brace-beam-column connections for concentrically braced frames with concrete filled tube columns," *Journal of Structural Engineering*, vol. 130, no. 2, pp. 233–243, 2004.
- [18] M. M. Hassan, H. M. Ramadan, M. Naeem, and S. A. Mourad, "Behavior of gusset plate-T0-CCFT connections with different configurations," *Steel and Composite Structures*, vol. 17, no. 5, pp. 735–751, 2014.
- [19] H.-T. Hu, C.-W. Chen, and M.-Y. Huang, "Nonlinear finite element analysis of CFT-to-bracing connections subjected to axial compressive forces," *Engineering Structures*, vol. 33, no. 5, pp. 1479–1490, 2011.
- [20] E. M. Hines, M. E. Appel, and P. J. Cheever, "Collapse performance of low-ductility chevron braced steel frames in moderate seismic regions," *AISC Engineering Journal*, vol. 46, no. 3, pp. 149–180, 2009.
- [21] C. D. Stoakes and L. A. Fahnestock, "Cyclic flexural testing of concentrically braced frame beam-column connections," *Journal of Structural Engineering*, vol. 137, no. 7, pp. 739–747, 2011.
- [22] C. D. Stoakes and L. A. Fahnestock, "Cyclic flexural analysis and behavior of beam-column connections with gusset plates," *Journal of Constructional Steel Research*, vol. 72, pp. 227–239, 2012.
- [23] S. Kishiki, S. Yamada, and A. Wada, "Experimental evaluation of structural behavior of gusset plate connection in BRB frame system," in *Proceedings of the 14th World Conference on Earthquake Engineering*, Beijing, China, October 2008.
- [24] CEN-1993-1-8 and Eurocode 3, "Design of steel structures," in *Part 1-8: Design of Joints*, European Committee for Standardization, Brussels, Belgium, 2005.
- [25] GB50011-2010, *Code for Seismic Design of Buildings*, China Architecture and Building Press, Beijing, China, 2010.
- [26] L.-H. Han, G.-H. Yao, and Z. Tao, "Performance of concrete-filled thin-walled steel tubes under pure torsion," *Thin-Walled Structures*, vol. 45, no. 1, pp. 24–36, 2007.
- [27] P. Wang, J. Pan, Z. Wang, and S. Chen, "Experimental and analytical behavior of stiffened angle joints," *Steel and Composite Structures*, vol. 26, no. 1, pp. 67–78, 2018.
- [28] S. Torabian, S. R. Mirghaderi, and F. Keshavarzi, "Moment-connection between I-beam and built-up square column by a diagonal through plate," *Journal of Constructional Steel Research*, vol. 70, no. 2, pp. 385–401, 2012.



Hindawi

Submit your manuscripts at
www.hindawi.com

